Comparison of Freehand 3D Ultrasound Calibration Techniques Using a Stylus

P-W. Hsu, G. M. Treece, R. W. Prager
N. E. Houghton and A. H. Gee

CUED/F-INFENG/TR 579

June 2007

University of Cambridge
Department of Engineering
Trumpington Street
Cambridge CB2 1PZ
United Kingdom

Email: pwh24@cam.ac.uk, gmt11/rwp/neh27/ahg @eng.cam.ac.uk

Comparison of Freehand 3D Ultrasound Calibration Techniques Using a Stylus

Po-Wei Hsu, Graham M. Treece, Richard W. Prager, Neil N. Houghton and Andrew H. Gee

University of Cambridge
Department of Engineering
Trumpington Street
Cambridge CB2 1PZ

Abstract

In a freehand 3D ultrasound system, a probe calibration is required to find the rigid body transformation from the corner of the B-scan to the electrical centre of the position sensor. The most intuitive way to perform such a calibration is by locating fiducial points in the scan plane directly with a stylus. The main problem of using this approach is the difficulty in aligning the tip of the stylus with the scan plane. The thick beam width makes the tip of the stylus visible in the B-scan even if the tip is not exactly in the elevational centre of the scan plane. In this paper, we present two novel phantoms that simplify the alignment process for more accurate probe calibration. We also compare our calibration techniques with a range of styli and show that our phantom outperforms other approaches in both accuracy and simplicity.

1 Introduction

Freehand three-dimensional (3D) ultrasound (Fenster et al., 2001) is a 3D medical imaging system with many clinical applications in anatomy visualization, volume measurements, surgery planning and radiotherapy planning (Gee et al., 2003). As a conventional two-dimensional (2D) ultrasound probe is swept over the anatomy of interest, the trajectory of the probe is recorded by the attached position sensor. The volume of the anatomy can be constructed by matching the ultrasonic data with its corresponding position in space. However, the position sensor measures the 3D location of the sensor S, rather than the scan plane P, relative to an external world coordinate system W as shown in Figure 1. It is therefore necessary to find the position and orientation of the scan plane with respect to the electrical centre of the position sensor. This rigid-body transformation $\mathrm{T}_{S \leftarrow P}$ is determined through a process called probe calibration. In general, a transformation involves both a rotation and a translation in 3D space. For brevity, we will use the notation $\mathrm{T}_{B \leftarrow A}$ to mean a rotational transformation followed by a translation from the coordinate system A to coordinate system B.

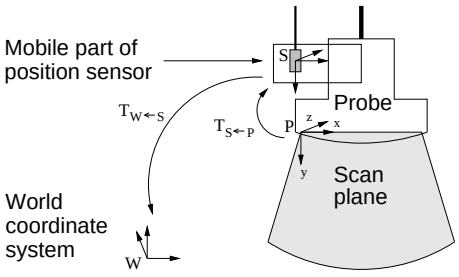

Figure 1: The coordinates associated with the scan plane and mobile part of the position sensor.

3D ultrasound calibration has been an active research topic for several years (Mercier et al., 2005). The usual approach is to scan an object with known dimensions (a phantom). These scans

place constraints on the six calibration parameters—3 translations in the direction of the x, y and z axes and the 3 rotations, azimuth, elevation and roll, about these axes.

The simplest phantom is probably a point target. This can be in the form of a cross-wire (Detmer et al., 1994; Gooding et al., 2005) or a small spherical ball bearing (State et al., 1994; Amin et al., 2001; Barratt et al., 2006). The point is scanned from different positions and orientations, and its location marked in the B-scans. The segmented points can be mapped to the sensor's coordinate system by using an assumed calibration and then to the world coordinate system from the position sensor readings. If the assumed calibration is correct, the points from the B-scans should have the same coordinates in 3D space. This places constraints on the calibration parameters. The calibration is solved by an iterative optimisation technique.

A 3D localizer, often called a pointer or a stylus, can be used to aid probe calibration. It is essentially a point target connected to another position sensor at the end of the stylus, which can be spherical or sharpened to a point. The rigid-body transform between the tip of the stylus and the position sensor is usually supplied by the manufacturer (Muratore and Galloway Jr., 2001). In the case where the transformation is not available, it can be determined by a simple pointer calibration (Leotta et al., 1997). During a pointer calibration, the stylus is rotated about its tip while the position sensor's readings are recorded. Since the tip of the stylus must be mapped to the same location in 3D space, this places constraints on the possible locations of the stylus's tip, whose location can be determined by an iterative optimisation algorithm. In any case, the location of the stylus's tip is known in 3D space. The location of the point phantom can therefore be determined by pointing the stylus at the phantom. If the scales of the B-scan are known (Hsu et al., 2006), the calibration parameters can be solved in a closed-form by least squares minimisation (Arun et al., 1987).

Calibrating with the point phantom has three major disadvantages. Firstly, it is very difficult to align the point phantom precisely with the scan plane. The finite thickness of the ultrasound beam makes the target visible in the B-scans even if the target is not exactly in the elevational centre of the scan plane. This error can be several millimetres depending on the ultrasound probe and the skill of the user. Secondly, automatic segmentation of isolated points in ultrasonic images is seldom reliable. As a result, the point phantom is often manually or semi-automatically segmented in the ultrasound images. This makes the calibration process long and tiresome. Finally, the phantom needs to be scanned from a sufficiently diverse range of positions, so that the resulting system of constraints is not under-determined with multiple solutions (Prager et al., 1998).

Over the last decade, much research has been undertaken to make probe calibration more reliable, and at the same time easier and quicker to perform. Prager et al. (1998) were the first to scan a plane instead of the point phantom. The design complexity of the plane varies from the floor of a water tank (Prager et al., 1998), a plexiglass plate (Rousseau et al., 2005), a nylon membrane (Langø, 2000) to a precision made Cambridge phantom (Prager et al., 1998). In each case, the plane appears as a straight line in the B-scans. This can be automatically segmented reliably to allow rapid calibration. Just as in the case of a point phantom, the segmented lines place constraints on the calibration parameters during the optimisation algorithm.

The main advantage of using a plane phantom is the time needed for calibration is shortened considerably. It is not necessary to align the probe with the phantom and the B-scan images can be segmented automatically. However, the plane needs to be scanned in a predefined configuration in order to constrain the calibration parameters. This requires the user to be skilled and experienced, even though a eigenvalue metric may be used to assess whether the calibration parameters are under-constrained (Hsu et al., 2006).

A different class of phantoms is the two-dimensional alignment phantom. Sato et al. (1998) aligned the scan plane with a thin board with three vertices. Each vertex is located in space with a stylus and segmented manually in the B-scans. The corresponding calibration can be solved in a closed-form as described previously. These phantoms have the advantage that only one frame is needed for probe calibration. Nevertheless, up to 20 frames may be necessary for an accurate calibration (Pagoulatos et al., 2001). The probe still needs to be aligned accurately with the phantom, which is very difficult with the thick ultrasound beam. The manual segmentation of the vertices means that calibration remained a lengthy process.

A Z-fiducial phantom is designed by Comeau et al. (1998) to solve the alignment problem in 2D phantoms. The phantom consists of wires or rods in a 'Z' shape. The intersection of the scan plane with these fiducials forms a virtual 2D phantom that can be used to define the position of the scan plane in space. The phantom itself is defined in space either by using a stylus (Pagoulatos et al., 2001; Hsu et al., 2007a) or using another position sensor (Bouchet et al., 2001; Lindseth et al., 2003; Chen et al., 2006). Automatic segmentation can be achieved by either reducing the design complexity of the phantom (Chen et al., 2006) or by the aid of an additional planar membrane (Hsu et al., 2007a). This allows calibration to be completed in a few seconds. However, the accuracy of such calibration remains poorer than other phantoms (Hsu et al., 2007a).

Gee et al. (2005) designed a mechanical device where the 2D phantom is aligned using micrometers. They mounted wedges onto the planar phantom so that any misalignment could be easily detected in the ultrasound images. These wedges also served as the fiducial points to be located in space, which are semi-automatically segmented. The phantom itself is not located in space using a stylus. Instead a gantry is designed so that both the position sensor and the probe can be precisely mounted onto the phantom.

It is possible to perform calibration by scanning a phantom and register the ultrasonic image with its geometric model. Blackall et al. (2000) registered the ultrasonic image of a gelatin phantom. The calibration parameters are found where the reconstructed phantom best fits the model. Dandekar et al. (2005) used two parallel wires to mimic a plane phantom. The virtual plane phantom is the unique plane that passes through the two wires. This phantom forego the automatic segmentation and subsequently the rapid calibration advantage of the plane phantom, but is still subject to the same disadvantages of using such phantoms. Both these techniques are time consuming.

Since a stylus can be used to locate points in 3D space, Muratore and Galloway Jr. (2001) calibrated their probe by locating points directly in the scan plane. Assuming at least 3 non-collinear points have been located, calibration can be solved by least squares optimisation as previously described. This technique nevertheless requires two targets to be tracked simultaneously. Furthermore, it is difficult to align the tip of the stylus with the scan plane.

Khamene and Sauer (2005) improved on this technique by imaging a rod transversely. Both ends of the rod are pointer calibrated to define the location and orientation of the rod in space. Each image of the rod sets up a constraint on the calibration parameters. Probe calibration can then be found using optimisation techniques.

In this paper, we study relative merits of a particular class of calibration algorithms that locate points in the B-scan with a stylus. We have designed two phantoms with similar designs. We have published a preliminary calibration result based on one of the phantoms (Hsu et al., 2007b). The second phantom is a modified stylus that can be used for accurate probe calibration.

2 Materials and Methods

2.1 The Calibration Phantoms

Figure 2 shows the five calibration phantoms. Figures 2(a) and (b) are standard Polaris (Northern Digital Inc., Canada) styli with a sharp and a spherical tip. Figure 2(c) shows a rod stylus similar to the one used by Khamene and Sauer (2005). Figure 2(d) and (e) shows the cone phantom and the Cambridge stylus that we have designed. These are the 5 phantoms that we will use for probe calibration comparison. During probe calibration, we will scan a point x that is on the phantom. This point $x^{P'} = (u, v, 0)^t$ can be segmented in the ultrasound image, where u and v are the column and row indices of the cropped image in pixels. This point should be changed to SI units by an appropriate scaling factor $\mathrm{T}_s = \begin{pmatrix} s_u & 0 & 0 \\ 0 & s_v & 0 \\ 0 & 0 & 0 \end{pmatrix}$, where s_u and s_v are the scales in millimetres per pixel to give $x^P = \mathrm{T}_s x^{P'}$. If the probe calibration $\mathrm{T}_{S \leftarrow P}$ is known, then the

segmented point can be mapped to world space by:

$$x^W = \mathrm{T}_{W \leftarrow S} \mathrm{T}_{S \leftarrow P} x^P, \tag{1}$$

where $\mathrm{T}_{W \leftarrow S}$ is given by the Polaris readings.

(a) Sharp Stylus (b) Spherical Stylus (c) Rod Stylus

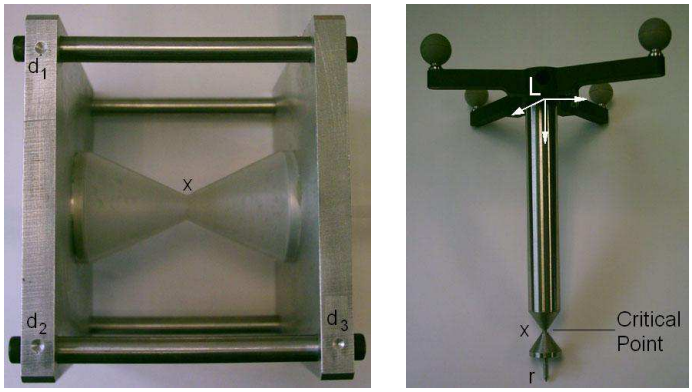

(d) Cone Phantom (e) Cambridge Stylus

Figure 2: The calibrations phantoms.

2.1.1 Polaris Styli

Figure 3 shows the coordinate systems involved when calibrating with either of the Polaris styli. During pointer calibration, the location of the stylus's tip x^L is found in the stylus's coordinate system L. This point can be mapped to 3D space by:

$$x^W = \mathrm{T}_{W \leftarrow L} x^L, \tag{2}$$

where the transformation $\mathrm{T}_{W \leftarrow L}$ can be read off the Polaris. If we place the stylus's tip in the scan plane, its location in space is given by Equation 1. This means that only the calibration $\mathrm{T}_{S \leftarrow P}$ and possibly the scale factors T_s are unknown in the two expressions for x^W. Calibration can therefore be found by equating Equations 1 and 2, i.e. minimizing

$$f_1 = f_2 = \sum_i \left| \mathrm{T}_{W \leftarrow S_i} \mathrm{T}_{S \leftarrow P} x_i^P - \mathrm{T}_{W \leftarrow L_i} x^L \right|, \tag{3}$$

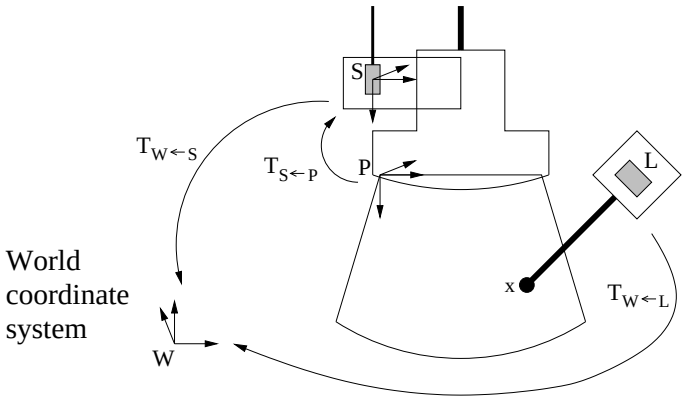

Figure 3: The coordinate systems involved when calibrating with a Polaris stylus.

where $|\cdot|$ denotes the usual Euclidean norm on $\mathbb{R}^3$. The above equation is minimized by using the iterative Levenberg-Marquardt algorithm (More, 1977).

2.1.2 Rod Stylus

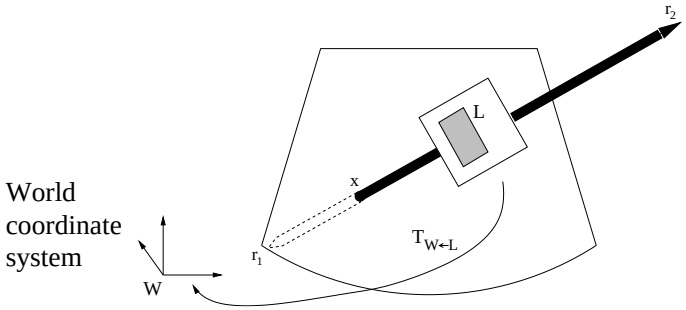

Figure 4: The coordinate systems involved when calibrating with a rod stylus.

Figure 2(c) shows the rod stylus that is used to follow the approach by Khamene and Sauer (2005). The corresponding coordinates are shown in Figure 4. We have attached a 15cm long, 1.5mm thick rod to a Polaris active marker. Both ends of the rod are sharpened for accurate pointer calibration. Again, the end points of the rod r_1^L and r_2^L are found by two separate pointer calibrations, and their coordinates in 3D space are $\mathrm{T}_{W\leftarrow L} r_1^L$ and $\mathrm{T}_{W\leftarrow L} r_2^L$ respectively. Now, the point of intersection of the rod and the scan plane is given by Equation 1. Furthermore, this point lies on the line formed by the two end points of the stylus. This means that the distance from the point x^W to the line $\overline{r_1^W r_2^W}$ is zero, i.e.

$$\begin{aligned} \frac{\left|\left(r_2^W - r_1^W\right) \times \left(r_1^W - x^W\right)\right|}{\left|r_2^W - r_1^W\right|} &= 0 \\ \Rightarrow \frac{\left|\left(\mathrm{T}_{W\leftarrow L} r_2^L - \mathrm{T}_{W\leftarrow L} r_1^L\right) \times \left(\mathrm{T}_{W\leftarrow L} r_1^L - \mathrm{T}_{W\leftarrow S}\mathrm{T}_{S\leftarrow P} x^P\right)\right|}{\left|\mathrm{T}_{W\leftarrow L} r_2^L - \mathrm{T}_{W\leftarrow L} r_1^L\right|} &= 0. \end{aligned} \tag{4}$$

The $\times$ in the above equations denotes the cross product of two vectors in $\mathbb{R}^3$. Calibration can be found by minimizing

$$f_3 = \sum_i \frac{\left|\left(\mathrm{T}_{W\leftarrow L_i} r_2^L - \mathrm{T}_{W\leftarrow L_i} r_1^L\right) \times \left(\mathrm{T}_{W\leftarrow L_i} r_1^L - \mathrm{T}_{W\leftarrow S_i}\mathrm{T}_{S\leftarrow P} x_i^P\right)\right|}{\left|\mathrm{T}_{W\leftarrow L_i} r_2^L - \mathrm{T}_{W\leftarrow L_i} r_1^L\right|}. \tag{5}$$

2.1.3 Cone Phantom

The cone phantom (Figure 2(d)) is primarily comprised of a polypropylene block machined into the shape of two hollow cones with 1mm wall thickness. The centre of the circle where the two cones join is the fiducial point x that we will use for probe calibration. If we view the cones longitudinally, the cones have diameters varying between 10mm and 50mm. The cones are supported by an aluminium frame structure consisting of two 135cm $\times$ 135cm square plates held together by four bolts. There are 3 cone-shaped divots d_i in the two blocks to fit a 3mm ball-pointed Polaris stylus. The position of the divots, d_i^W, are therefore known in 3D space. These divots serve as the principal axes of the phantom and are used to determine the phantom position in 3D space. The location of x is measured with a Mitutoyo (Mitutoyo Corporation, Japan) coordinate measuring machine (CMM) relative to the divots, i.e. $x^A = f_{\text{CMM}}(d_i^A)$, where the function f_{CMM} is determined by the coordinate measuring machine and is valid for arbitrary coordinate system A. In particular, $x^W = f_{\text{CMM}}(d_i^W)$ in world space. All dimensions are precision manufactured by our workshop with a tolerance of $\pm$0.1mm.

If we align the scan plane with the circle where the two cones join, we get a circle with a 12mm diameter. This circle can be segmented with its centre $x^{P'}$ automatically. As we shall see later, the image scales are necessary for reliable segmentation. Let us assume for the moment that the scales T_s are known, hence $x^P = \mathrm{T}_s x^{P'}$ can be computed.

Now, recall that we have already found the coordinates of this centre in 3D space. We can transform this point to the sensor's coordinate system by using the inverse of the position sensor's readings:

$$\begin{aligned} x^S &= \mathrm{T}_{W\leftarrow S}^{-1} x^W \\ &= \mathrm{T}_{W\leftarrow S}^{-1} f_{\text{CMM}}(d_i^W). \end{aligned} \tag{6}$$

For probe calibration, we need to find the single transformation $\mathrm{T}_{S\leftarrow P}$ that best transforms $\{x^{P_i}\}$ to $\{x^{S_i}\} = \{\mathrm{T}_{W\leftarrow S_i}^{-1} f_{\text{CMM}}(d_i^W)\}$. This can be found (Arun et al., 1987) by minimizing

$$f_4 = \sum_i \left| \mathrm{T}_{W\leftarrow S}^{-1} f_{\text{CMM}}(d_i^W) - \mathrm{T}_{S\leftarrow P} x^{P_i} \right|.$$

2.1.4 Cambridge Stylus

Figure 2(e) shows a photograph of our new Cambridge stylus. It consists of a stainless steal shaft, 120mm in length and 13mm in diameter. On one end of the shaft, a platform is ground to fit a PassTrax (Traxtal Technologies, Canada) position sensor in such a way that the z axis of the sensor is parallel to the shaft. The other end of the shaft is sharpened for accurate pointer calibration. As above, this means that the point r^L is found by a pointer calibration. The main feature of this stylus is that part is thinned in the shape of two cones, to meet at the critical point x. This point is precisely 20mm above the stylus's tip. Here, the diameter is 1.5mm. The stylus was precision manufactured by our workshop with a tolerance of $\pm$0.1mm.

From the geometric model of the stylus, $x^L = r^L - (0, 0, 20)^t$. We now place fiducial marks by aligning this critical point with the scan plane. From here, the calibration process is identical as with a Polaris stylus. The only difference been that we are aligning the critical point, and not the stylus's tip. The calibration parameters are found by minimizing

$$f_5 = \sum_i \left| \mathrm{T}_{W\leftarrow S_i} \mathrm{T}_{S\leftarrow P} x_i^P - \mathrm{T}_{W\leftarrow L_i} \left(r^L - (0, 0, 20)^t \right) \right|. \tag{7}$$

2.2 Segmentation

Figure 5 shows typical ultrasound images of the various phantoms. In Figures 5(b), (c) and (e), where the point of the stylus we are imaging is round, an umbrella shaped scatter can be seen clearly. This is due to the ultrasound deflecting off the curved surface. We will use this fact to segment the top of the imaged surface.

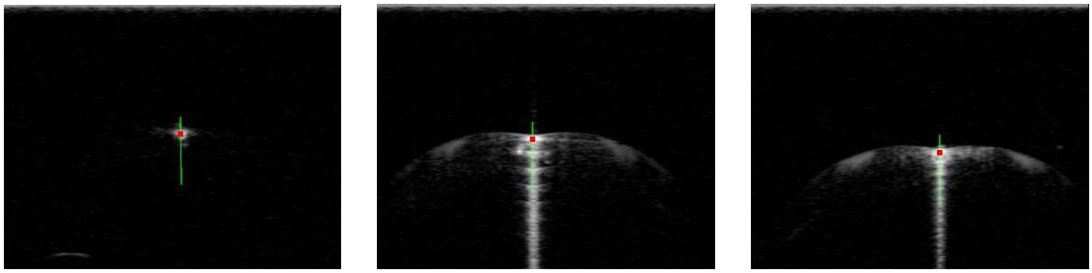

(a) Sharp Stylus (b) Spherical Stylus (c) Rod Stylus

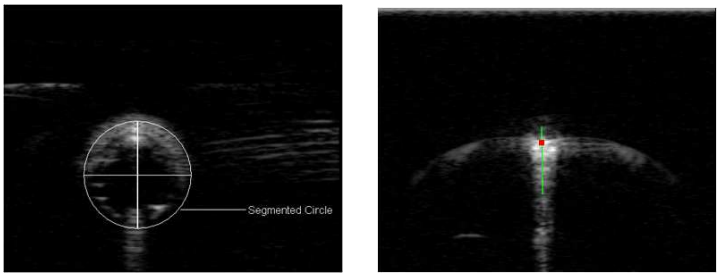

(d) Cone Phantom (e) Cambridge Stylus

Figure 5: Typical images of the different phantoms with the segmentation result imposed.

To begin with, we search through the entire image to find the pixel with maximum intensity. This pixel serves as a starting point for the segmentation algorithm. As we are anticipating an umbrella shaped response, there should be a near-vertical line of symmetry. We iterate this line through all possible angles, and across a horizontal distance about 10% of the image width, near the pixel with maximum intensity. The angles are incremented in steps of 1°. During each iteration, the correlation of the image on either side of the line is computed. Once we have found the line of symmetry corresponding to the maximum symmetric auto-correlation, the required point is assumed to be on this line. We search for consecutive pixels on this line that have a high intensity, with a preference given to pixels near the top of the line. This algorithm is used to segment the image of each stylus, and the results imposed on Figures 5(a)–(c) and (e). The line of symmetry is shown as well. Since the top, rather than the centre, of the surface is segmented, the correction is performed in the optimisation process to shift the segmented point downwards by half the stylus thickness. We have measured the spherical tip of the Polaris stylus to be 3.0mm in diameter with a digital micrometer. The thickness of the rod and Cambridge stylus is 1.5mm.

In order to allow calibration in cold water, we now post-process the segmented points by shifting them upwards towards the probe face. Assuming that the user will measure the water temperature, the speed of sound in water at this temperature can be computed (Bilaniuk and Wong, 1993). We then shift the pixels upwards by the temperature correction factor $\frac{\text{sound speed in water}}{1540}$.

For the cone phantom, we first place a user defined threshold on the B-scan to remove any unwanted scatters, resulting in a binary image consisting mainly of the circle that is to be segmented. We now shift each pixel upwards by the temperature correction factor. Edge detection is performed by applying a Sobel filter to overlapping 3×3 blocks of the image. If the image scales are known, we can apply the Hough transform (Hough, 1959) on the resulting edges to detect a circle with a 12mm diameter.

3 Results

In order to measure the calibration quality of the different phantoms, we calibrated a Diasus (Dynamic Imaging Ltd., U.K.) 5–10MHz linear-array probe. The analog radio-frequency (RF)

ultrasound data, after receive focusing and time-gain compensation but before log-compression and envelope detection, was digitized using a Gage CompuScope (Gage Applied Technologies Inc., U.S.A.) 14100 PCI 14-bit analog to digital converter, and transferred at the PAL rate of 25 frames per second to a Pentium(R) 4 2.80GHz PC running Microsoft Windows XP. Since we have access to the RF data, the image scales could be set at our discretion. The B-scans were displayed at 0.1mm/pixel, with a cropped size of 3.00mm × 3.81mm. The probe was tracked using a PassTrax (Traxtal Technologies, Canada) target for the Polaris (Northern Digital Inc., Canada) optical tracking system.

A pointer calibration was initially performed on each stylus. Five probe calibrations were followed by locating 20 points spread throughout the image by the stylus during each calibration. This whole routine was again repeated five times, each time with a different pointer calibration, as shown in Figure 6.

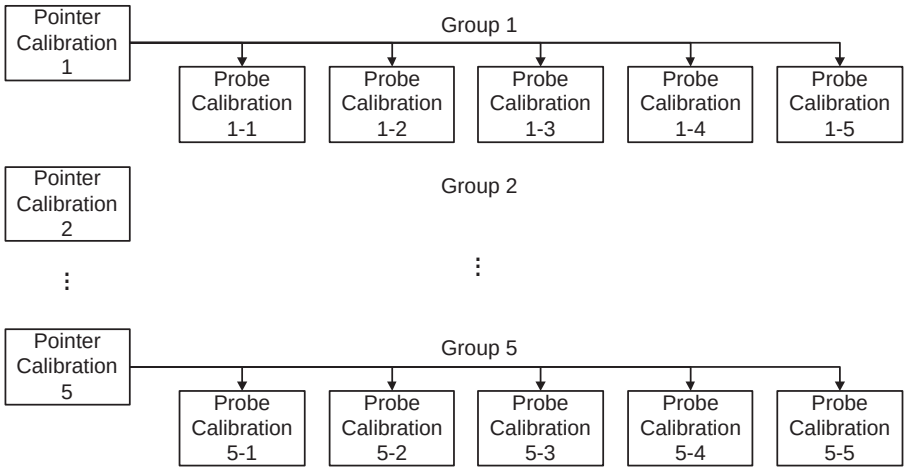

Figure 6: The calibration protocol. Five pointer calibrations were performed. For each pointer calibration, five probe calibrations were performed.

For probe calibrations with the cone phantom, a pointer calibrated stylus (Figure 2 (b)) was used to locate the phantom in space. Ten readings were taken at each divot, and the mean was used for probe calibration. Five calibrations, each with 20 images of the cone spread throughout the B-scan, were performed. Again, this process was repeated five times. Each time re-calibrating the stylus and relocating the phantom by its divots. Thus, a total of 25 calibrations was computed for each phantom.

3.1 Precision

One way to assess the calibration quality is by computing its precision. A point p^P in the scan plane can be mapped to the sensor's coordinate system after probe calibration, since $p^S = \mathrm{T}_{S \leftarrow P} p^P$. If all the calibrations are identical, the point p^S should remain stationary. Precision is therefore measured by calculating

$$\mu = \frac{1}{N} \sum_{i=1}^{N} \left(p^{S_i} - \overline{p^{S_i}} \right),$$

where p^{S_i} is the point in the sensor's coordinate system mapped by the i^{th} calibration, $\overline{p^{S_i}}$ is used to denote the arithmetic mean of $\left(p^{S_i}\right)$ and N is the number of calibrations. It is obvious that the above measure is dependent on the point chosen in the B-scan. We will therefore measure the variation of the four corners and the centre of the B-scan.

In order to investigate whether the pointer calibration is sufficiently accurate and measure its impact on the calibration result, we compute two precision measures. First, the precision for each

group of the five calibrations specific to the same pointer calibration is calculated. These five precisions for the five groups of calibrations are then averaged. Specifically,

$$\mu_1 = \frac{1}{25}\sum_{j=1}^{5}\sum_{i=1}^{5}\left(p_j^{S_i} - \overline{p_j^{S_i}}\right),$$

where $p_j^{S_i}$ denotes the point mapped by the i^{th} probe calibration associated with the j^{th} pointer calibration, and $\overline{p_j^{S_i}}$ is the mean of $\left(p_j^{S_1}, p_j^{S_2}, \cdots, p_j^{S_5}\right)$, for a given j. The results are shown in Table 1. Table 2 shows the precision without differentiating the 25 calibrations, i.e.

$$\mu_2 = \frac{1}{25}\sum_{i=1}^{25}\left(p^{S_i} - \overline{p^{S_i}}\right).$$

All units are in millimetres. The mean of the variation of the four corners and the centre of the B-scan is also given in the same table.

Table 1: Precision of the probe calibrations specific to each stylus pointer calibration.

Point	**Sharp**	**Spherical**	**Rod**	**Cone**	**Cambridge**
Top left	0.52	0.53	4.35	0.33	0.50
Top right	0.53	0.51	1.31	0.53	0.54
Bottom left	0.53	0.54	1.61	1.06	0.55
Bottom right	0.47	0.47	1.55	0.85	0.47
Centre	0.51	0.51	1.46	0.40	0.51
Mean	0.51	0.51	2.06	0.63	0.51

Table 2: Precision of undifferentiated probe calibrations.

Point	**Sharp**	**Spherical**	**Rod**	**Cone**	**Cambridge**
Top left	0.64	0.57	4.36	0.39	0.63
Top right	0.64	0.45	4.38	1.09	0.71
Bottom left	0.55	0.40	5.69	0.96	0.71
Bottom right	0.72	0.45	5.77	0.47	0.58
Centre	0.50	0.31	5.02	0.22	0.45
Mean	0.61	0.44	5.04	0.63	0.62

3.2 Accuracy

While precision measures calibration reproducibility, this does not reflect the accuracy of the calibration, since there may be a systematic error. We assess the accuracy of our calibrations by measuring the point reconstruction accuracy of a point target. We scan the tip of a wire that is 1.5mm thick in water at room temperature. The image of the wire tip is reconstructed in space by using the obtained calibrations. The 3D location of the wire tip is found by using an independent stylus. Ten readings were obtained to eliminate errors from the stylus's readings. Accuracy is measured by the amount of mismatch between the reconstructed image and the mean of the stylus's readings.

Point reconstruction accuracy may be dependent on the position of the probe and the position of the wire tip in the B-scan. We therefore capture images of the wire tip at five different locations in the B-scans—near the four corners and the centre of the B-scan. The probe is also rotated

about the lateral axis at six different locations. Furthermore, five images of the wire are taken at each probe position and at each location in the B-scans. A total of 150 images of the wire tip are captured. The point reconstruction accuracy is shown in Table 3, where the figures shown are the mean of the 30 repetitions at each position in the B-scan in millimetres.

Table 3: Point reconstruction accuracy of the calibrations.

Point	**Sharp**	**Spherical**	**Rod**	**Cone**	**Cambridge**
Top left	4.09	4.26	8.22	2.25	2.78
Top right	3.68	3.72	7.51	2.19	2.43
Bottom left	2.77	3.44	7.85	1.89	1.94
Bottom right	2.86	3.68	7.89	2.39	2.21
Centre	2.65	3.07	7.25	1.84	1.52

4 Discussions

From the precision measures, we see that the rod stylus performs considerably worse than the other 4 phantoms. The precision is similar for these four phantoms irrespective of which precision measure is used. This means that the pointer calibrations for these styli are sufficiently accurate and have a limited effect on calibration precision. For the rod stylus, there is a discrepancy between the two precision measures. This means that although for a particular pointer calibration, a precision of about 2mm can be achieved, a significant worse precision of 5mm should be expected when given an arbitrary probe calibration.

The relatively high error in the point reconstruction accuracy using the calibrations from the rod stylus further suggests that such a phantom is unreliable for probe calibration. Both the sharp and spherical stylus have similar point reconstruction accuracies, been slightly worse than the cone phantom and Cambridge stylus. This difference is mainly attributed to the fact that it is difficult to align the scan plane with the tip of the sharp and spherical styli. Even though the spherical stylus produces a better reflection, which can suggest whether we have aligned its tip correctly, this information is found to be unhelpful as the calibration accuracies have not been improved. Both the cone phantom and the Cambridge stylus produce the best accuracies since any misalignment of the phantom with the scan plane is readily visible in the B-scans.

Although precision and accuracy may be the most important measures to judge a calibration technique, there are other factors that should be noted. Firstly, the image scales need to be known in order to segment the circle for the cone phantom. We have this information because we have access to the RF data. This may not be the case for other research groups, in which case the scales may need to be determined by another technique, such as using the distance measurement tool (Hsu et al., 2006). The ultrasonic settings such as transmitter and receiver gain and time gain compensator need to be set manually by the user for optimal segmentation. The user also needs to ensure that the correct circle has been segmented by the algorithm, reject and repeat any obvious incorrect segmentations.

The stylus has the advantage that segmentation is not highly dependent on the ultrasound machine settings. The image scales can also be formed part of the optimisation process, when functions $f_1 = f_2, f_3, f_5$ are minimized. However, it appears that function f_3 has multiple local minima. In our calibrations, it is necessary to fix the image scales and choose a starting point sufficiently near the solution for the optimisation to converge to the correct minimum. Nevertheless, since the phantom does not need to be aligned with the scan plane, calibration is easy and rapid to perform.

A summary of the various factors that should be taken into account when choosing a calibration technique is given in Table 4. This table is drawn up based our experiences from working with these phantoms. All the factors are graded into five classes: very poor, poor, moderate, good

and very good, except the need for the image scales, which is simply classed as required or not required.

Table 4: Probe calibration factors.

Factor	**Sharp**	**Spherical**	**Rod**	**Cone**	**Cambridge**
Precision	Good	Good	Very poor	Good	Good
Accuracy	Moderate	Moderate	Very poor	Good	Good
Image scales	Not required	Not required	Required	Required	Not required
Easy to use	Easy	Easy	Very easy	Moderate	Easy
Rapid calibration	Rapid	Rapid	Very rapid	Moderate	Rapid
Reliability	Very Reliable	Very reliable	Very unreliable	Reliable	Very reliable
Easy to make	Very easy	Very easy	Very easy	Moderate	Easy

From the table it can be deduced that the rod stylus lies at one end of the scale, offering speed and simplicity as its main advantages, but failing to ensure a reliable, precise and accurate calibration. The cone phantom is an improvement on the sharp and spherical stylus, but the phantom is considerably larger and requires more skill to use it. The Cambridge stylus clearly surpasses the other styli, offering better accuracy and retaining calibration simplicity.

5 Conclusion

We have compared different techniques to calibrate freehand 3D ultrasound probes using a stylus. The rod stylus is very simple and quick to use, but produces very poor precision and accuracy. This phantom may be useful to obtain a quick estimate of the calibration, although this may be needed in the first place for the optimisation when using such a phantom. The cone phantom produces better calibration accuracies at the expense of a more sophisticated phantom, segmentation and calibration protocol. The Cambridge stylus is clearly an improvement on both the sharp and the spherical stylus with a small modification to the design. Better accuracies are achieved, while maintaining its ease of use and calibration simplicity. Both the cone phantom and the Cambridge stylus produces similar calibration precision and accuracy. The Cambridge stylus is smaller in size and easier to manufacture. On the other hand, the Cambridge stylus is limited to specific position sensing devices that can be mounted with its z axis parallel to the shaft of the stylus. One advantage of the cone phantom over every styli is that calibration does not require two targets to be tracked simultaneously.

References

D. V. Amin, T. Kanade, B. Jaramaz, A. M. DiGioia III, C. Nikou, R. S. LaBarca, and J. E. Moody Jr. Calibration method for determining the physical location of the ultrasound image plane. In *Proceedings of the 4th International Conference on Medical Image Computing and Computer-Assisted Intervention, Lecture Notes in Computer Science*, volume 2208, pages 940–947. Springer, 2001.

K. S. Arun, T. S. Huang, and S. D. Blostein. Least-squares fitting of two 3-D point sets. *IEEE Transactions on Pattern Analysis and Machine Intelligence*, 9(5):698–700, 1987.

D. C. Barratt, G. P. Penney, C. S. K. Chan, C. M. Slomczykowski, T. J. Carter, P. J. Edwards, and D. J. Hawkes. Self-calibrating 3D-ultrasound-based bone registration for minimally invasive orthopedic surgery. *IEEE Transactions on Medical Imaging*, 25(3):312–323, 2006.

N. Bilaniuk and G. S. K. Wong. Speed of sound in pure water as a function of temperature. *The Journal of the Acoustical Society of America*, 93(3):1609–1612, 1993.

J. M. Blackall, D. Rueckert, C. R. Maurer Jr., Hill D. L. G. Penney, G. P., and D. J. Hawkes. An image registration approach to automated calibration for freehand 3D ultrasound. In *Proceedings of the 3rd International Conference on Medical Image Computing and Computer-Assisted Intervention, Lecture Notes in Computer Science*, volume 1935, pages 462–471. Springer, 2000.

L. G. Bouchet, S. L. Meeks, G. Goodchild, F. J. Bova, J. M. Buatti, and W. A. Friedman. Calibration of three-dimensional ultrasound images for image-guided radiation therapy. *Physics in Medicine and Biology*, 46:559–577, 2001.

T. K. Chen, P. Abolmaesumi, A. D. Thurston, and R. E. Ellis. Automated 3D freehand ultrasound calibration with real-time accuracy control. In *Proceedings of the 9th International Conference on Medical Image Computing and Computer-Assisted Intervention, Lecture Notes in Computer Science*, volume 4190, pages 899–906. Springer, 2006.

R. M. Comeau, A. Fenster, and T. M. Peters. Integrated MR and ultrasound imaging for improved image guidance in neurosurgery. In *Proceedings of SPIE*, volume 3338, pages 747–754, 1998.

S. Dandekar, Y. Li, J. Molloy, and J. Hossack. A phantom with reduced complexity for spatial 3-D ultrasound calibration. *Ultrasound in Medicine & Biology*, 31(8):1083–1093, 2005.

P. R. Detmer, G. Bashein, T. Hodges, K. W. Beach, E. P. Filer, D. H. Burns, and D. E. Stradness Jr. 3D ultrasonic image feature localization based on magnetic scanhead tracking: in vitro calibration and validation. *Ultrasound in Medicine & Biology*, 20(9):923–936, 1994.

A. Fenster, D. B. Downey, and H. N. Cardinal. Three-dimensional ultrasound imaging. *Physics in Medicine and Biology*, 46:R67–R99, 2001.

A. H. Gee, R. W. Prager, G. H. Treece, and L. H. Berman. Engineering a freehand 3D ultrasound system. *Pattern Recognition Letters*, 24:757–777, 2003.

A. H. Gee, N. E. Houghton, G. M. Treece, and R. W. Prager. A mechanical instrument for 3D ultrasound probe calibration. *Ultrasound in Medicine & Biology*, 31(4):505–518, 2005.

M. J. Gooding, S. H. Kennedy, and J. A. Noble. Temporal calibration of freehand three-dimensional ultrasound using image alignment. *Ultrasound in Medicine & Biology*, 31(7):919–927, 2005.

P. V. C. Hough. Machine analysis bubble chamber pictures. In *International Conference on High Energy Accelerators and Instrumentation*, pages 554–556. CERN, 1959.

P-W. Hsu, R. W. Prager, A. H. Gee, and G. M. Treece. Rapid, easy and reliable calibration for freehand 3D ultrasound. *Ultrasound in Medicine & Biology*, 32(6):823–835, 2006.

P-W. Hsu, R. W. Prager, A. H. Gee, and G. M. Treece. Real-time freehand 3D ultrasound. *Ultrasound in Medicine & Biology*, Submitted, 2007a.

P-W. Hsu, R. W. Prager, N. E. Houghton, A. H. Gee, and G. M. Treece. Accurate fiducial location for freehand 3D ultrasound calibration. In *Proceedings of SPIE*, volume 6513, 2007b.

A. Khamene and F. Sauer. A novel phantom-less spatial and temporal ultrasound calibration method. In *Proceedings of the 8th International Conference on Medical Image Computing and Computer-Assisted Intervention, Lecture Notes in Computer Science*, volume 3750, pages 65–72. Springer-Verlag, 2005.

T. Langø. *Ultrasound guided surgery: image processing and navigation.* PhD thesis, Norwegian University of Science and Technology, Trondheim, Norway, 2000.

D. F. Leotta, P. R. Detmer, and R. W. Martin. Performance of a miniature magnetic position sensor for three-dimensional ultrasound imaging. *Ultrasound in Medicine & Biology*, 23(4): 597–609, 1997.

F. Lindseth, G. A. Tangen, T. Langø, and J. Bang. Probe calibration for freehand 3-D ultrasound. *Ultrasound in Medicine & Biology*, 29(11):1607–1623, 2003.

L. Mercier, T. Langø, F. Lindsesth, and D. L. Collins. A review of calibration techniques for freehand 3-D ultrasound systems. *Ultrasound in Medicine & Biology*, 31(4):449–471, 2005.

J. J. More. The Levenberg-Marquardt algorithm: implementation and theory. In *Numerical Analysis, Lecture Notes in Mathematics*, volume 630, pages 105–116. Springer-Verlag, 1977.

D. M. Muratore and R. L. Galloway Jr. Beam calibration without a phantom for creating a 3-D freehand ultrasound system. *Ultrasound in Medicine & Biology*, 27(11):1557–1566, 2001.

N. Pagoulatos, D. R. Haynor, and Y. Kim. A fast calibration method for 3-D tracking of ultrasound images using a spatial localizer. *Ultrasound in Medicine & Biology*, 27(9):1219–1229, 2001.

R. W. Prager, R. N. Rohling, A. H. Gee, and L. Berman. Rapid calibration for 3-D freehand ultrasound. *Ultrasound in Medicine & Biology*, 24(6):855–869, 1998.

F. Rousseau, P. Hellier, and C. Barillot. Confhusius: A robust and fully automatic calibration method for 3D freehand ultrasound. *Medical Image Analysis*, 9(1):25–38, 2005.

Y. Sato, M. Nakamoto, Y. Tamaki, T. Sasama, I. Sakita, Y. Nakajima, M. Monden, and S. Tamura. Image guidance of breast cancer surgery using 3-D ultrasound images and augmented reality visualization. *IEEE Transactions on Medical Imaging*, 17(5):681–693, 1998.

A. State, D. T. Chen, C. Tector, A. Brandt, H. Chen, R. Ohbuchi, M. Bajura, and H. Fuchs. Case study: observing a volume rendered fetus within a pregnant patient. In *Proceedings of the Conference on Visualization '94, IEEE Visualization*, pages 364–368, California, 1994. IEEE Computer Society Press.